Journal Pre-proof

Synthesis of active electrocatalysts using glycine–nitrate chemistry

Atul P. Jamale, A. Natoli, Lata D. Jadhav

Please cite this article as: A.P. Jamale, A. Natoli, L.D. Jadhav, Synthesis of active electrocatalysts using glycine–nitrate chemistry, *Journal of Physics and Chemistry of Solids* (2020), doi: https://doi.org/10.1016/j.jpcs.2020.109723.

This is a PDF file of an article that has undergone enhancements after acceptance, such as the addition of a cover page and metadata, and formatting for readability, but it is not yet the definitive version of record. This version will undergo additional copyediting, typesetting and review before it is published in its final form, but we are providing this version to give early visibility of the article. Please note that, during the production process, errors may be discovered which could affect the content, and all legal disclaimers that apply to the journal pertain.
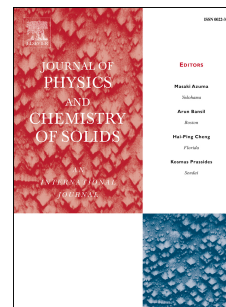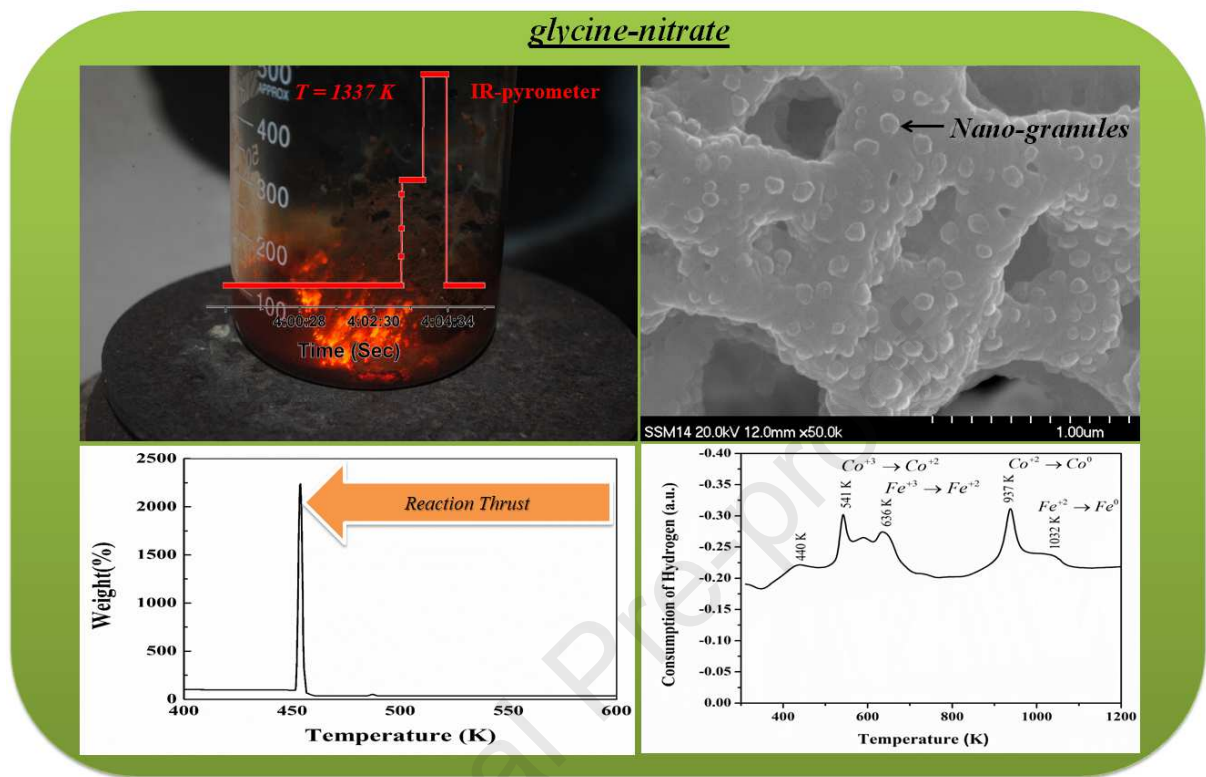
CrediT authorship contribution statement

Atul Jamale: Writing original draft, writing review and editing **A. Natoli:** Formula analysis, visualization **Lata Jadhav:** conceptualization, methodology

Graphical abstract:

Fig. 1: Glycine-nitrate propellant chemistry for synthesis of predominant surface area materials.

Synthesis of active electrocatalysts using glycine–nitrate chemistry

Atul P. Jamale[a,b*], A. Natoli[a], Lata D. Jadhav[c]

[a]Department of Materials and Ceramic Engineering, CICECO, University of Aveiro, Santiago University Campus, 3810-193 Aveiro, Portugal

[b]Department of Physics, Shivaji University, Kolhapur 416004, India

[c] Electrochemical Energy Materials Laboratory, Department of Physics, Rajaram College, Kolhapur, 416 004, India

Abstract

Due to sluggish oxygen reduction reactions, development in the solid oxide fuel cell (SOFC) field is stagnant. Two solutions, increasing the active surface or use of precious materials, can stimulate the oxygen reduction kinetics on electrodes. Thus, to gain both these benefits, the present article addressed the synthesis of high surface-area mixed oxide ionic–electronic conductor $La_{0.6}Sr_{0.4}Co_{0.8}Fe_{0.2}O_{3-\delta}$ (LSCF) using chemistry of the propellant glycine–nitrate reaction. In this study, different fuel to oxidant ratios (ψ), 2.0, 2.6, and 3.0 were used to control the exothermicity of reaction and powder properties. The maximum reaction temperature of 1337 K at $\psi = 3.0$ resulted in coarsened powder. In contrast, comparatively less exothermicity of reaction at $\psi = 2.0$ resulted in powder with substantial Brunauer–Emmett–Teller surface area of 10.97 $m^2 g^{-1}$, with maximum powder compaction achieved at sintering of 1273 K. With optimal direct current in-plane electrical conductivity of 341 S cm^{-1}, H_2-temperature-programmed reduction showed excellent catalytic activity for the sample obtained at $\psi = 2.0$. The electrochemical performance comparisons of electrodes in two different cell geometries – with and without a gold catalytic current collecting layer (Au–CCCL) – revealed the least polarization and cell resistance in the cell with Au–CCCL. The electrode area specific resistance and cell conductivity using Au–CCCL were 0.097 Ω cm^{-2} and 0.15 S cm^{-1}, respectively.

Keywords: Solid oxide fuel cell; Glycine–nitrate process; H_2-temperature-programmed reduction; Electrode; Electrochemical performance

Corresponding Author

Dr. Atul P. Jamale

Department of Materials and Ceramic Engineering,

CICECO, University of Aveiro, Santiago University Campus,

3810-193 Aveiro, Portugal

+351-913102633

jamaleatul@gmail.com

atuljamale@ua.pt

1. Introduction

The miniaturization capability and advanced physicochemical properties of nanoparticles has led to rapid growth in nanotechnology in science and technology. Nanotechnology offers a cost-effective approach to assemble devices due to the requirement of less materials and lower associated cost. On a particle scale, nanoparticles are fundamentally different from micron sizes of a fixed composition in regard to advanced electrical, mechanical, thermal, optical, structural, and catalytic properties [1–6]. However, an extraordinary behavior of nanoparticles due to predominance of surface agglomeration during high-temperature processing, making extended durable applications impractical [4]. Therefore, scientific research in energy conversion and storage technologies is stagnant concerning synthesis of pure and stable nanoparticles for supercapacitors, batteries, and solid oxide fuel cells (SOFCs). Due to considerable fuel to electrical energy conversion efficiency and environmentally benign properties, SOFCs are attracting global attention [7]. Nevertheless, SOFC technology is not yet commercialized, due to some critical issues – for example, reduced lifetime due to chemical compatibility among SOFC components, inadequate densification of electrolyte mixing the oxidizing and reducing gases prior to cell reaction, inferior electrolyte conductivity, and mediocre activity of electrodes for redox reactions of the respective gases remain unsolved [8]. Simultaneously working on all these aspects is, however, very complex, and the current topic is restricted to synthesis of catalytically active nanocrystalline electrodes.

Reducing degradation owing to cross-over diffusion and overall system cost are key in SOFC research, which includes checking various possibilities to decrease operation temperature to as low as 773–973 K [9–11]. For a given oxide ion conducting electrolyte of few micron thickness, the activation loss over an oxygen electrode is significant, limiting the low-temperature goal. Numerous attempts have been made using classical electronically conducting Pt-metal and $La_{(1-X)}Sr_XMnO_{3-\delta}$, and were found wanting due to restricted oxygen reduction reaction (ORR) at the electrode–electrolyte interface [12]. In such material, the entire electrode volume is rarely utilized during operation and, for effective operation, the entire electrode should be in active mode. The material $La_{0.6}Sr_{0.4}Co_{0.8}Fe_{0.2}O_{3-\delta}$ (LSCF) is one potential mixed oxide ion electronic conducting electrode material and solution, extending the ORR from electrode–electrolyte to electrode–gas interface due to additional oxide ion diffusion paths [13,14]. Further improvement can be made by reducing the particles to nano size.

The methodologies normally used to synthesize nanoparticles are categorized as top-down and bottom-up approaches. In the top-down approach, the nanostructure components are considered as a basic building block of superstructure, whereas in the latter the atoms or molecules self-assemble to build a nanostructure. The bottom-up approaches, including the glycine–nitrate process (GNP), co-precipitation, sonochemical, spray drying, mechanochemical, and reverse missiles are all cost-effective compared with top-down approaches [15]. However, synthesizing a considerable amount of the multi-metal oxides of perovskite, fluorite, and pyrochlore families is more complicated than for single component metal oxides. Thus, GNP was chosen over bottom-up approaches for the synthesis of nanomaterial. The several advantages of GNP – for example, simple and relatively fast process to obtain the stoichiometric materials at a molecular level, and no requirement of sophisticated instrument and hence economically affordable – are gaining much attention from researchers. The GNP is based on propellant chemistry, in which reaction exothermicity is principally balanced by changing the stoichiometry among oxidizing and reducing agents [16–18].

Depending on material processing, the nature of nanocrystalline powder, and hence the electrocatalytic oxygen reduction properties of material in the ultimate application, change. Recently, combustion synthesis has become a common method for perovskite and double-perovskite synthesis, with differences only in the varieties of fuel – e.g. urea [18,19], glycine [17–20], citric acid [18,21,22], ethylene glycol [23], sucrose [24], and alanine [25] – used during synthesis. The synthesis based on propellant chemistry is a thermally induced redox reaction with reaction exothermicity, and is determined by fuel type and fuel to oxidant ratio [19,26]. The synthesis is completed in a few minutes and produces large volumes of gaseous products, which isolates the nanoparticles and so prevents them agglomerating. Thus, type of fuel and oxidizer [16,19,27], ignition temperature [28], and fuel to oxidant ratio (ψ) [16] are principal parameters determining the purity, morphology, and crystallite and particle sizes of powder. Among various salts used as an oxidizer, the metal nitrates remain the first preference because the rapid oxidizing capability and higher degree of water solubility maintain the solution homogeneity at the molecular level [29]. The fuel was selected by fulfilling specific requirements, e.g. maximum gas evolution following reaction, good chelation ability, low ignition temperature, and high exothermicity of fuel [26]. Due to good complexing ability of the carbonyl group and vigorous triggering of combustion reaction on the amino group [30], the existence of both groups is essential for maximum fuel benefit.

4

Among the frequently studied glycine (NH_2CH_2COOH), urea [$CO(NH_2)_2$], and citric acid [$HOC(CH_2)_2(COOH)_3$] fuels, glycine is exceptionally good because it has both carbonyl and amino groups at the end of the structure. Considering the above merits, metal nitrate and glycine were chosen as oxidizer and fuel precursors, respectively, comprising GNP.

In the present research, ignition temperature (575 K) and type of fuel and oxidizer were kept constant, and synthesis was performed under fuel-deficient, stoichiometric, and fuel-rich conditions of ψ to determine the effect on adiabatic temperature of combustion reaction and physiochemical properties of powders. Because as-synthesized powders include carbon and unburned fuel residues, an intermediate calcination is recommended in most studies to remove these organic entities [21,25,31–33]. However, these volatile and uniformly distributed impurities in powders oxidize easily in atmospheric air sintering. Further, due to coherence of impurities with carbon black pore former, usually obtained in incomplete or partial combustion of hydrocarbons and petroleum products, the existence of some impurities may produce a porous structure [34,35]. Thus, to take advantage of volatile impurities as pore formers and to minimize the intermediate calcination stage, the as-synthesized powder was compacted and consolidated in one-step sintering. The consolidated samples were then analyzed for structural, morphological, and electrochemical properties.

2. Experimental

The nanocrystalline LSCF was thoroughly synthesized by the facile GNP, using the nitrate-based precursors of La, Sr, Co, and Fe metal ions, and glycine as a propellant. All nitrates were analytical grade, and ionized in doubled distilled water to the required stoichiometry. The resulting solution was stirred constantly with the dropwise addition of glycine stock solution to provide ψ of 2.0, 2.6, and 3.0. The solution was then heated slowly to transform the entire mass into transparent gel and then combusted at 573 K on a pre-heated hot plate. The synthesis details were provided in an earlier publication [17]. Here, the effect of organic residue on properties of electrode is studied. The carbon and residual fuel of the as-synthesized powders were eliminated during sintering at 1273 K. The in-situ removal of organic impurities has two purposes: (i) reduction of several heat treatments to a single step and (ii) CO_x gas released in partial oxidation of carbon generates the porous microstructure, essential in the diffusion and distribution of the gas phase in electrodes of SOFC. For convenience, the powders synthesized at different ψ of 2.0, 2.6, and 3.0 are abbreviated as L20, L26, and L30, respectively, and corresponding sintered bodies are L20S, L26S, and L30S.

The high-temperature GNP evolves a tremendous quantity of gas, which conducts the heat away from the reaction. Hence, the combustion reaction is not exactly adiabatic but exchanges part of the heat with the surrounding gaseous atmosphere and container. Consequently, the reaction temperature drops below the ideal thermodynamic value. The actual temperature and moles of gases taking part in the reaction at different ψ were inspected using IR-pyrometer (AST MT500) and thermogravimetric analysis (TGA, SDT Q600 V20.9 Build 20) instruments, respectively. The observations made in both analyses support the comment that "temperature deviation of the combustion reaction from the adiabatic value is due to increased quantity of gases at higher ψ." The particle growth under reaction enthalpy was also evaluated in a dynamic laser scattering experiment (Malvern 4800 Autosizer) and performed on a suspension prepared in double distilled water. Alternatively, the particle growth for individual ψ was visualized using field-emission scanning electron microscopy (FE-SEM, JEOL JSM-6500) equipped with energy dispersive spectroscopy (EDS). The specific surface areas and pore size distributions of powders obtained at various ψ were evaluated using a Brunauer–Emmett–Teller (BET) analyzer. After performing fundamental characterizations on powders, L20 powder was analyzed using transmission electron microscopy (TEM) and H_2-temperature-programmed reduction setup (H_2-TPR, Zeton Altamira AMI-200) to determine the oxygen activities within the temperature range of SOFC.

The sintered samples were examined for phase purity using an X-ray diffractometer (XRD, Bruker D2-Phaser), with diffraction angle $2\theta = 20$–$80°$ and step size of $0.02°$. The surface of the optimized sample was scanned for chemical state and composition determination using X-ray photoelectron spectroscopy (XPS). The extreme fuel-deficient and fuel-rich samples were chosen for direct current (DC) in-plane electrical conductivity measurement using the van der Pauw four-probe technique. For a measurement, a constant current of 40 mA was passed through two probes, and the resulting potential drop across the remaining probes was measured using an electronic multimeter. The measurements on all samples were performed in identical conditions, in static air, and within the temperature range of 298–1023 K.

3. Results and discussion

3.1. Powder characterization

High-temperature thermo-chemical and thermo-mechanical failures are challenges for prolonged operation and commercialization of SOFC technology. Hence, research is focused on decreasing the operation temperature to a usable level. Consistent with the research

indicators, an alternative electrode material with least polarization and ohmic losses is of major importance and is the aim in preparation of catalytically active and advanced nanocrystalline materials.

The catalytic activity is work function dependent, and can mainly be tuned by altering particle size, external electrical field, or switching to new chemical composition of materials [36,37]. Thus, the work function is the least amount of energy required to release an electron from the cathode surface in reducing gaseous oxygen to oxide ions and then incorporating them into the lattice. To serve the catalyst goal, the mixed ionic–electronic conductor (MIEC) LSCF was selected and synthesized thoroughly by GNP at different ψ. A large amount of energy is released in synthesis as shown by the flame in the reaction mixture of **Fig. 1**. Temperature of the reaction mixture or flame is demonstrated in the temperature versus time profile (**Fig. 2a**). The progressively increasing temperature with fuel amount (**Table 1)** explains the C, H, and O abundance. At the fuel-deficient ratio, the oxidizing species are though sound good, the reducing species required to complete the combustion deflated, making it difficult to reach the optimum temperature. However, an increased amount of fuel in stoichiometric and fuel-rich conditions respectively shifts the mode of reaction from partial to complete combustion, and accordingly the temperature of reaction rises. The maximum temperature is for reaction at ψ = 3.0 (1337 K), which is still lower than the value estimated from an adiabatic reaction [17]. The significant deviation in reaction temperature may due to the dissipation of heat by the large volume of gas evolved in the reaction, which is very large for the higher fuel amount. These gases exert thrust at the bottom of the combustion vessel and blow a small quantity of powder. Similar thrusts are also observed in TGA of the precursor (**Fig. 2b**), showing the weight gain about an ignition temperature of glycine of 453 K. The magnitudes of thrust observed in synthesis of L26 and L30 powders are 6.6 and 22.4 times that gained in L20 synthesis, respectively, supporting the comment that "increased gaseous quantity in combustion at higher fuel amount determines the temperature of reaction mixture and properties of final powders."

The high-temperature results in particle agglomeration. However, the soft and loosely bonded agglomerates formed at lower ψ can disperse on sonication and hence improve the electrocatalytic applicability [38,39]. In electrochemistry, the electrochemical processes function due to the active sites available for reactions – they are much higher for materials of huge surface areas, which provide a large number of dangling electrons while tightly bonded bulk electrons remain isolated [40]. Thus, the electrode surface determines the activity,

mainly due to large numbers of unpaired surface electrons, and hence performance during application in SOFC. In the present study, the specific surface areas of materials are estimated from the N_2-adsorption–desorption experiment. The adsorption–desorption isotherms and pore distributions obtained in experiments are presented in **Fig. 3**. The isotherms resemble the H1/H2-hysteresis of the IUPAC standard and of areas demonstrating high specific surface areas. The shape of the curve denotes the mesoporous powder generated as a consequence of random access of gas in combustion [41].

The N_2-adsorption on the walls of pores results in the sluggish increment in adsorption (**Fig. 3**). The adsorption reaches a plateau at about $P/P_0 = 0.70$. At $P/P_0 > 0.70$, further adsorption follows the nitrogen condensation in pores. Thus, the estimation of adsorbed and desorbed nitrogen species gives the average specific surface area of samples and it is shown in **Table 1**. The maximum surface area is obtained for the L20 sample, which is the result of decreased reaction temperature due to voluminous gas products. These gas products restrict direct contact among the particles and hence material sintering [19]. For $\psi >$ 2.0, the gas products are not effective in overcoming the sintering, resulting in materials of minimum surface area. The pore size distribution in **Fig. 3** illustrates peak maxima at about 21, 16, and 14 nm for L20, L26, and L30, respectively. The maximum pore volume of 4.95×10^{-4} cm^3 $gm^{-1} nm^{-1}$ occurs for the L20 sample with average pore diameter of about 21 nm. The maximum pore volume is the consequence of lower reaction temperature and simultaneously less gas evolution by combustion at a lower ψ. Whereas, in the cases of $\psi =$ 2.6 and 3.0, the increased reaction temperature eliminates the effect of gaseous products and densifies the fluffy foam. These results are consistent with FE-SEM images showing dual-scale morphology, the foam-like interconnected networks with overgrown particles (**Fig. 4**). The dual-scale morphology with co-existing larger size voids reflects the quantity of gas expelled in combustion, which is larger with increasing amount of fuel [27]. However, the local sintering due to the temperature generated in combustion at an elevated fuel level is unavoidably accompanied by overgrown particles of size 100 nm (**Fig. 4d**). Thus, sintering of the interconnected network with accommodation of larger particles is truly a high-temperature phenomenon [19]. Further, the TEM analysis across particles of interest demonstrates the highly oriented crystalline planes (**Fig. 4e**). These planes are 0.272 nm apart and are assigned to d_{104} interplanar spacing of L20. The close matching of d_{104} values obtained for TEM and XRD techniques (**Table 2**) implies that a nanocrystalline

rhombohedral perovskite is formed in as-synthesized powders with inevitable residual carbon.

The catalytic activity is defined by presence of peroxides, superoxide, hydroxyl radical, singlet oxygen, and alpha-oxygen species. Thus, to elucidate the chemical environment (hydroxide or carbonate species) of material, the oxide ionic mobility was studied under a reducing atmosphere and within SOFC operating temperatures. It has been well established that oxide ions diffuse along surface, grain-boundary, and lattice pathways, and these are categorized depending on the nature of diffusion as $\alpha 1$-, $\alpha 2$- and β-oxygen, respectively. Under partial reducing conditions, the loosely bonded chemisorbed $\alpha 1$-oxygen condensed on the surface of the materials eliminates vigorously during the initial stage of heating, whereas $\alpha 2$-oxygen bonded with trivalent Co and Fe in vicinity of grain-boundaries eliminates at a later stage. The lattice β-oxygen is strongly bonded and participates in the diffusion process only at elevated temperature. Thus, detailed knowledge of degree of $\alpha 1$-, $\alpha 2$-, and β-oxygen and temperature of activation helps in calibration of the surface and bulk oxide ionic diffusivity of electrodes, and hence the applicability of materials over a temperature range.

Since catalytic activity is surface dependent, only the sample with high specific surface area of $10.97 \ \mathrm{m^2 \, g^{-1}}$ was chosen. The oxygen activity resolved under a 10% H_2 + 90% Ar atmosphere and at constant flow of $50 \ \mathrm{cm^3 \, min^{-1}}$ is shown in **Fig. 5**. The H_2-TPR result demonstrates two sets of major signals (accompanying several minor kinks) respectively within two temperature ranges, 523–673 and 773–1073 K. The few minor peaks also occur in the low-temperature region, explaining the $\alpha 1$-oxygen condensed in the carbonate or hydroxide forms. The first set of major peaks (523–673 K) represent contemporaneous $Co^{3+} \rightarrow Co^{2+}$ and $Fe^{3+} \rightarrow Fe^{2+}$ charge transfer reactions, whereas the second set (773–1073 K) of $Co^{2+} \rightarrow Co^0$ and $Fe^{2+} \rightarrow Fe^0$ transformations are attributed to semiconductor to metallic-like transition [42]. Thus, the reduction of cations to lower oxidation state accompanies the H_2-consumption owing to $\alpha 1$-, $\alpha 2$-, and β-oxygen species active in a respective temperature range; and the area of individual peaks quantifies the corresponding oxygen loss, foremost for lattice oxygen at about 937 K. The quality of H_2-TPR in combination with an earlier O_2-TPO result [17] indicates the potential of LSCF for use as an electrode in symmetrical SOFC.

3.2. Characterization of sintered samples

Because high-temperature performance of SOFCs is sensitive to impurities, the materials being considered should be pragmatically diagnosed. The X-ray crystallographic

study was carried out on all samples sintered at 1273 K for 2 h. The obtained data are indexed and compared with ICDD 00-048-0124 (**Fig. 6**). The reflections (012), (104), (202), (024), (116), (300), (208), and (128) at the Bragg's diffraction angles of 23.17°, 32.98°, 40.59°, 47.31°, 53.28°, 58.81°, 69.16°, and 78.79°, respectively, confirm that all samples are of rhombohedral perovskite structure (space group R-3c) and no remnant carbon or secondary impurities occur within the resolution limit of technique. The crystallite sizes and X-ray and Archimedes densities are all summarized in **Table 2,** demonstrating the dominance of high surface area samples. The X-ray and Archimedes densities both show similar trends with maxima for L20S.
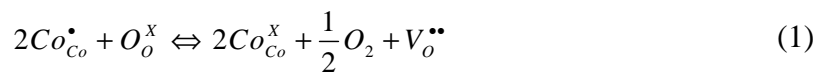
The densification is essentially determined by the presence of organic impurities, initial particle size, and material sinterability [43]. It should be recalled that all samples have identical chemical composition and hence common sinterability behavior, and so particle size and degree of leftover organic impurities become the only factors determining sample compaction. The powders synthesized at low ψ acquire high specific surface area and consequently the particles are smaller. Hence, higher compressibility and inter-particle reactivity of the green body due to improved contact among the fine nano-sized particles eliminates the intermittences at moderate sintering temperature. In contrast, the powder synthesis at higher ψ results in harder and coarser particles separated by much larger voids. Additionally, the powder synthesis at higher ψ adds a significant amount of carbon residue, which produces CO_x gas during sintering. The evolved gases and presence of such intrusions hinder the densification to much higher temperatures [44]. Thus, the sample acquiring larger particles and organic impurities retains the porous microstructure, which results in inferior densification for powders obtained at high ψ.

The SEM topography of samples sintered at 1273 K for 2 h shows compact morphology for L20S, but L26S and L30S contain larger and non-uniform particle distributions (**Fig. 7**). Additionally, the hexagonal rods found on the surface and bulk of L20 remain a mystery. The rods are ~1 μm long and 50–280 nm wide (**Fig. 7d and e**). The elemental analysis (**Fig. 8** and **Table 3**) shows that the rods are composed of La, Sr, Co, and Fe cations, but with different stoichiometry to the precursor (3:2:4:2). A Sr-rich surface is proposed on the basis of cationic radii, composition, and oxo-basicity. Due to size misfit of A-site dopants (r_{Sr} = 149 pm, r_{La} = 115 pm) and at extensive Sr-doping (≥0.4), the LSCF perovskite remains under lattice strain. In addition to lattice strain (a driving force responsible for diffusion of cations) due to misfit of A-site dopant and Sr-doping above a threshold limit,

the unbalanced chemical potential due to surface vacancies drags the alkaline solutes to the surface, effectively maintaining equilibrium.

Alkaline and rare earths have a stronger diffusion propensity in neutralization, forming the less reliable $Re_2O_2(CO_3)$ and $Re(OH)_3$ products on exposure to air, CO_2, or a hydrated atmosphere [31]. The sensitive XPS technique was utilized in quantification of the chemical composition, electronic states of constituents, and extents of chemisorbed and lattice oxygen species of the surface. The chemical composition determined from the full width at half maxima peak intensities is given in **Table 3,** exhibiting the deviation from precursor stoichiometry with the Sr-rich surface.

The C1s, La3d, Sr3d, Co2p, Fe2p and O1s XPS spectra are shown in **Fig. 9**. For the analysis, the Cls peak located at 284.4 eV is used as a reference. The deconvolution of the O1s peak is ascribed to the lattice (O^{2-}) and chemisorbed (O^-) species at the binding energies (BEs) of 527.6 and 530.1 eV, respectively [45]. The chemisorbed species indicate the strongly interacting surface oxide ionic vacancies. Thus, the ratio among chemisorbed to total oxygen content determines the degree of surface oxygen vacancies and hence the surface exchange kinetics, which is 56.63% in the present case. Such a large ratio may also result from the additional basicity contribution due to Sr-enrichment at $Sr \geq 0.4$, which leads to a lower La/Sr ratio (**Table 3**). Within the range of $0.1 > x < 0.4$, when Sr^{2+} is substituted with La^{3+} in perovskite structure of LSCF, the oxidation state of the B-site cation varies from tri- to tetra-valence in maintaining charge neutrality. However, B^{4+} is not a normal oxidation state and releases oxygen in achieving the stable B^{3+} (i.e. formation of oxide vacancy by eq. 1 and 2). Additionally, higher composition and relatively less oxygen affinity (covalent characteristic) of Co makes the oxygen desorption easier compared to Fe [33].

$$2Co_{Co}^{\bullet} + O_O^X \Leftrightarrow 2Co_{Co}^X + \frac{1}{2}O_2 + V_O^{\bullet\bullet} \tag{1}$$

$$2Fe_{Fe}^{\bullet} + O_O^X \Leftrightarrow 2Fe_{Fe}^X + \frac{1}{2}O_2 + V_O^{\bullet\bullet} \tag{2}$$
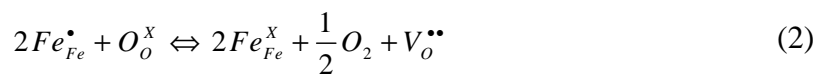
The chemical composition reveals a Sr-rich surface, which responds readily to atmospheric CO_2 or H_2O [46,47]. Thus, for each $Sr3d_{3/2}$ and $Sr3d_{5/2}$ core-level spectra, the spin-orbital doublets corresponding to normal Sr^{2+} state (134.7 and 135.9 eV) and state owing to charge transfer among the strontium and CO^{3-} or OH^- ligands (132.4 and 133.9 eV) are expected [48]. Types of doublets have also been reported for $La3d_{3/2}$ and $La3d_{5/2}$ core-levels, first at the BEs of 832.2 and 850.4 eV, and second at 834.7 and 852.1 eV, respectively [49].

However, the peak intensities corresponding to CO^{3-} or OH^- species are lower, illustrating the surface deficiency of La.

The BE for $Co2P_{3/2}$ and $Co2P_{1/2}$ core-levels are 777.9 and 792.8 eV, respectively, with no shake-up contribution, evidencing the low spin Co(III) [31]. Because the Fe composition is lower, the peak intensities corresponding to $Fe2P_{5/2}$ and $Fe2P_{3/2}$ are inferior. Furthermore, the BE gap of 10.6 eV indicates low spin Fe(III), and no shake-up contribution due to CO^{3-} or OH^- species.

Fig. 10 shows the logarithmic DC in-plane electrical conductivity of extreme samples measured as a reciprocal function of temperature. Due to less oxide ionic transport, the major portion of the electrical conductivity measured with the van der Pauw technique may be regarded as electronic. The conductivity plots show the Arrhenius trend to 873 K, which decreases with further rises in temperature. The conduction within the Arrhenius region is due to polaron hopping in the B–O–B electrical branch, which principally depends on the degree of overlapping of the 3d-transition metal orbital and the 2P-orbital of oxygen [33]. However, the high-temperature deviation (≥873 K) is explained by the oxygen loss (generation of oxide ion vacancy) owing to semiconductor to metallic-like transition. These thermally induced vacancies hamper the charge carrier hole concentration and mobility [50]. These results are consistent with those of XPS and H_2-TPR, and show the maximum electrical conductivity, 341 S cm^{-1} at 873 K, is achieved only in L20S. The maximum conductivity is attributed to the connectivity improvement due to compressibility of nanoparticles. The activation energy of L20S calculated within 623–873 K is $E_a = 4.05$ kJ mol^{-1}, lower than the values reported in single-phase LSCF and composite with gadolinium-doped ceria electrolyte [32,51].

3.3. Electrochemical characterization of L20S

In the ORR evaluation, electrochemical impedance spectroscopy (EIS) measurement was performed on electrodes in ambient air. All measurements were performed in a symmetrical cell with the $Ce_{0.9}Gd_{0.1}O_{1.95}$ (CGO) electrolyte, already sintered at 1823 K for 4 h. The L20S sample, selected on the basis of highest DC conductivity, was pulverized and then deposited on CGO by the thick film screen-printing technique. The preparation of slurry, thick film deposition, and fabrication of the symmetrical cell are all described in a previous publication [52]. Special care was also taken to minimize ambiguity because of particle coarsening during the second time of consolidation in thick film, which was done at 1173 K for 2 h, lower than the previously attempted sintering condition in densification of L20S.

The lower in-plane electric conductivity greatly lowered ORR, deviating the electrode features from the standard SOFC, in which the additionally used catalytic current collecting layer (CCCL) [53] and interconnectors [54,55] are believed to promote the ORR due to augmented electron transport through. Therefore, the two distinct experiments, with and without use of CCCL, were conducted to match the coherence with SOFC. In previous study, priority was given to Au over Pt, Ag, and Pd metals, as other metals are recognized electrodes and known for overwhelming ORR in low-temperature fuel cells [56–58], which increases the complexity in assessment of activity due to MIEC. Curled Au-wire was also used to carry the electronic current from electrode surface to the EIS instrument.

The electrode activity was determined in a symmetrical cell using an EIS (HP 4284A LCR Meter) instrument, within SOFC working temperatures of 873–1073 K, and at intervals of 25 K (frequencies from 20 Hz to 1 MHz, and at a constant rms voltage of 0.5 V). The spectra, initially corrected and normalized for lead Au-wire resistances and electrode area, respectively, were analyzed using Z-view software (Scriber Associates Inc). The method is effective in separating the different electrochemical processes, e.g. adsorption and dissociation of oxygen by charger transfer reaction, oxygen gas and oxide ionic diffusions in electrode, and then ionic transport across the electrode–electrolyte interface of the device. Each process has a fixed time constant ($\tau = RC = 1/f_r$) related to the specific resistances (R) and capacitances (C), resonating at frequency f_r. Thus, stimulation of the device over a frequency range gives tentative information about the active processes.

For convenience and to minimize complexity, the Nyquist plots of L20 electrodes in two different geometries are presented alone in **Fig. 11a**, and the rest of the data are displayed in terms of the temperature-dependent electrode area specific resistance (ASR) and cell conductivity. As depicted in the inset of **Fig. 11a**, an equivalent circuit consisting of a series resistance (R_e), inductance (L), and the two parallel branches of constant phase elements CPE_{ct} and CPE_{diff} and resistances R_{ct} and R_{diff}, respectively corresponding to the charge transfer reaction and ionic diffusion processes, was used to fit the data. The spectra are depressed and deconvoluted into the processes mentioned above using complex non-linear least square fitting (**Fig. 11a**). All fittings overlapping exactly to the spectra implies the lowest electrode ASR for L20 with Au–CCCL. Alternatively, the performance augmentation can also be envisaged from the ohmic resistance references of the cells prior to and after Au–CCCL application.

The dependence of electrode polarization resistance on applied current and potential has been studied for electrode materials [59–61]. The results of earlier studies showed disturbed current distribution in electrode and electrolyte of the cell due to higher in-plane resistance and discrete connectivity due to porous structure of electrode affecting the polarization and cell resistances. Due to higher in-plane resistance [62,63], the bare L20S fails to distribute the electrons uniformly throughout the structure, resulting in only a small part of the electrode surface enabling the ORR and then oxide ionic transport through the electrode and electrolyte components. In contrast, the increased contact area between electrode and CCCL reduces the in-plane resistance. Thus, Au–CCCL not only improves ORR but also the consequential oxide ionic diffusion through electrode and electrolyte, clearly shown in the high frequency intercepts on the Z-axis of the EIS (**Fig. 11a**).

The ASR and cell conductivity are all thermally activated, and therefore the fitting outcomes are illustrated simply in terms of temperature dependence in **Fig. 11b**. An exponential ASR decay is a characteristic of charge transfer and ionic diffusion relaxion processes with increasing temperature. A substantial ASR difference is found between bare L20S and L20S with Au–CCCL. In fact, the gap reduces drastically at higher temperatures. At higher temperatures, the increased conductivity due to localized semiconductor (thermally activated carrier hopping with charge fluctuations on transition Co and Fe metals) to delocalized metal-like transition of LSCF accelerates ORR [64,65]. Interestingly such a transition in LSCF cannot exceed the electrical conductivity of Au metal (~10^5 S cm^{-1} [66]) [33]. In addition to relatively lower electrical conductivity, the porous microstructure of L20S leads to poorer and uneven current distribution in electrode and electrolyte of the cell [67]. This poorer and uneven voltage or current distribution affects the ionic diffusion through the cell and hence overall conductivity. A similar response is also seen in the net conductivity of cell, in which the resistive contribution is mainly due to more difficult ionic transport in the electrolyte component of the cell. At 1073 K, the measured cell conductivity using the L20S electrode with Au–CCCL is 0.15 S cm^{-1}, almost four-fold that of the cell with bare L20S. The ASR and activation energy of L20S with Au–CCCL are 0.097 Ω cm^{-2} at 1073 K and 146.66 kJ mol^{-1}, respectively. The activation energy is well within the 133.15–159.2 kJ mol^{-1} spectrum reported for an analogous system in electrochemical studies [61,68–70].

4. Conclusion

In the present investigation, the reaction kinetics of GNP are shown in detail for synthesis of nanocrystalline materials. This time-saving and efficient approach can produce a

multi-metal oxide powder with considerable surface area in its as-synthesized form. The data acquired in measurement of reaction temperature in an IR-pyrometer shows that the combustion clearly deviates from an adiabatic nature with a higher ψ. Due to less exothermicity of reaction at a lower ψ, the powder synthesis at limited fuel exposure, for example at $\psi = 2.0$, leads to weakly bonded agglomerates that are active enough to reduce the molecular oxygen into radicals. The higher catalytic activity of nanocrystalline powder is shown by the area of H_2-TPR peaks, which originate as the charge transfer reaction consequences of transition metals in low and high temperature bands.

The organic residual impurities of as-synthesized powders are used as a pore former in the second half of the study. This results in a porous microstructure, with higher electrode porosity for the samples prepared from powders synthesized at increasingly higher ψ. The porosity effect is also noticeable in DC in-plane electrical conductivity of samples, with highest electrical conductivity in L20S due to less residual carbon and higher compressibility of the nanoparticles. Despite variable porosity, all the samples surpass the electrical conductivity requirement of 100 S cm^{-1}. The electrochemical studies on L20S in two different configurations (with and without use of Au–CCCL) show the oxygen reduction capacity of the electrode surface. The study sets an additional constraint of CCCL requirement for the application of LSCF in low-temperature SOFCs – meaning that a LSCF electrode alone is not sufficient for low-temperature uses.

Acknowledgment

References

[1]   A. V. Vorontsov, S. V. Tsybulya, Influence of nanoparticles size on XRD patterns for small monodisperse nanoparticles of CuO and TiO$_2$ anatase, Ind. Eng. Chem. Res. 57

(2018) 2526–2536. doi:10.1021/acs.iecr.7b04480.

[2]   M.I. Pryazhnikov, A. V. Minakov, V.Y. Rudyak, D. V. Guzei, Thermal conductivity measurements of nanofluids, Int. J. Heat Mass Transf. 104 (2017) 1275–1282. doi:10.1016/j.ijheatmasstransfer.2016.09.080.

[3]   J. Lv, J. Yang, X. Li, Z. Chai, Size dependent radiation-stability of ZnO and TiO_2 particles, Dye. Pigment. 164 (2019) 87–90. doi:10.1016/j.dyepig.2019.01.014.

[4]   M.A. Ashraf, W. Peng, Y. Zare, K.Y. Rhee, Effects of size and aggregation/agglomeration of nanoparticles on the interfacial/interphase properties and tensile strength of polymer nanocomposites, Nanoscale Res. Lett. 13 (2018). doi:10.1186/s11671-018-2624-0.

[5]   T.V.S.L. Satyavani, B. Ramya Kiran, V. Rajesh Kumar, A. Srinivas Kumar, S. V. Naidu, Effect of particle size on dc conductivity, activation energy and diffusion coefficient of lithium iron phosphate in Li-ion cells, Eng. Sci. Technol. Int. J. 19 (2016) 40–44. doi:10.1016/j.jestch.2015.05.011.

[6]   L. Bai, X. Wang, Q. Chen, Y. Ye, H. Zheng, J. Guo, Y. Yin, C. Gao, Explaining the size dependence in platinum-nanoparticle-catalyzed hydrogenation reactions, Angew. Chemie - Int. Ed. 55 (2016) 15656–15661. doi:10.1002/anie.201609663.

[7]   A. Baldinelli, L. Barelli, G. Bidini, Performance characterization and modelling of syngas-fed SOFCs (solid oxide fuel cells) varying fuel composition, Energy. 90 (2015) 2070–2084. doi:10.1016/j.energy.2015.07.126.

[8]   L. Fan, B. Zhu, P.C. Su, C. He, Nanomaterials and technologies for low temperature solid oxide fuel cells: recent advances, challenges and opportunities, Nano Energy. 45 (2018) 148–176. doi:10.1016/j.nanoen.2017.12.044.

[9]   Z. Gao, L. V. Mogni, E.C. Miller, J.G. Railsback, S.A. Barnett, A perspective on low-temperature solid oxide fuel cells, Energy Environ. Sci. 9 (2016) 1602–1644. doi:10.1039/c5ee03858h.

[10]   Q.L. Liu, K.A. Khor, S.H. Chan, High-performance low-temperature solid oxide fuel cell with novel BSCF cathode, J. Power Sources. 161 (2006) 123–128.

doi:10.1016/j.jpowsour.2006.03.095.

[11] X. Zhang, L. Liu, Z. Zhao, B. Tu, D. Ou, D. Cui, X. Wei, X. Chen, M. Cheng, Enhanced oxygen reduction activity and solid oxide fuel cell performance with a nanoparticles-loaded cathode, Nano Lett. 15 (2015) 1703–1709. doi:10.1021/nl5043566.

[12] M. Gödickemeier, K. Sasaki, L.J. Gauckler, I. Riess, Electrochemical characteristics of cathodes in solid oxide fuel cells based on ceria electrolytes, J. Electrochem. Soc. 144 (1997) 1635–1646. doi:10.1149/1.1837653.

[13] F. Tietz, V.A.C. Haanappel, A. Mai, J. Mertens, D. Stöver, Performance of LSCF cathodes in cell tests, J. Power Sources. 156 (2006) 20–22. doi:10.1016/j.jpowsour.2005.08.015.

[14] D. Beckel, U.P. Muecke, T. Gyger, G. Florey, A. Infortuna, L.J. Gauckler, Electrochemical performance of LSCF based thin film cathodes prepared by spray pyrolysis, Solid State Ion. 178 (2007) 407–415. doi:10.1016/j.ssi.2007.01.019.

[15] A. Biswas, I.S. Bayer, A.S. Biris, T. Wang, E. Dervishi, F. Faupel, Advances in top-down and bottom-up surface nanofabrication: Techniques, applications & future prospects, Adv. Colloid Interface Sci. 170 (2012) 2–27. doi:10.1016/j.cis.2011.11.001.

[16] H. Fathi, S.M. Masoudpanah, S. Alamolhoda, H. Parnianfar, Effect of fuel type on the microstructure and magnetic properties of solution combusted Fe_3O_4 powders, Ceram. Int. 43 (2017) 7448–7453. doi:10.1016/j.ceramint.2017.03.017.

[17] A.P. Jamale, S. Shanmugam, C.H. Bhosale, L.D. Jadhav, Physiochemical properties of combustion synthesized $La_{0.6}Sr_{0.4}Co_{0.8}Fe_{0.2}O_{3-\delta}$ perovskite: a role of fuel to oxidant ratio, Mater. Sci. Semicond. Process. 40 (2015) 855–860. doi:10.1016/j.mssp.2015.07.091.

[18] C. Zhu, A. Nobuta, I. Nakatsugawa, T. Akiyama, Solution combustion synthesis of $LaMO_3$ (M = Fe, Co, Mn) perovskite nanoparticles and the measurement of their electrocatalytic properties for air cathode, Int. J. Hydrogen Energy. 38 (2013) 13238–13248. doi:10.1016/j.ijhydene.2013.07.113.

[19] S. Hadke, M.T. Kalimila, S. Rathkanthiwar, S. Gour, R. Sonkusare, A. Ballal, Role of fuel and fuel-to-oxidizer ratio in combustion synthesis of nano-crystalline nickel oxide powders, Ceram. Int. 41 (2015) 14949–14957. doi:10.1016/j.ceramint.2015.08.037.

[20] Q. Xu, D. ping Huang, F. Zhang, W. Chen, M. Chen, H. xing Liu, Structure, electrical conducting and thermal expansion properties of $La_{0.6}Sr_{0.4}Co_{0.8}Fe_{0.2}O_{3-\delta}$-$Ce_{0.8}Sm_{0.2}O_{2-\delta}$ composite cathodes, J. Alloys Compd. 454 (2008) 460–465. doi:10.1016/j.jallcom.2006.12.132.

[21] L. Ge, Z. Zhu, Z. Shao, S. Wang, S. Liu, Effects of preparation methods on the oxygen nonstoichiometry, B-site cation valences and catalytic efficiency of perovskite $La_{0.6}Sr_{0.4}Co_{0.2}Fe_{0.8}O_3-\delta$, Ceram. Int. 35 (2009) 3201–3206. doi:10.1016/j.ceramint.2009.05.024.

[22] J. Park, J. Zou, H. Yoon, G. Kim, J.S. Chung, Electrochemical behavior of $Ba_{0.5}Sr_{0.5}Co_{0.2-x}Zn_xFe_{0.8}O_3 -\delta$ (x = 0-0.2) perovskite oxides for the cathode of solid oxide fuel cells, Int. J. Hydrogen Energy. 36 (2011) 6184–6193. doi:10.1016/j.ijhydene.2011.01.142.

[23] D.M. Bastidas, S. Tao, J.T.S. Irvine, A symmetrical solid oxide fuel cell demonstrating redox stable perovskite electrodes, J. Mater. Chem. 16 (2006) 1603–1605. doi:10.1039/b600532b.

[24] L. da Conceição, A.M. Silva, N.F.P. Ribeiro, M.M.V.M. Souza, Combustion synthesis of $La_{0.7}Sr_{0.3}Co_{0.5}Fe_{0.5}O_3$ (LSCF) porous materials for application as cathode in IT-SOFC, Mater. Res. Bull. 46 (2011) 308–314. doi:10.1016/j.materresbull.2010.10.009.

[25] A. Dutta, J. Mukhopadhyay, R.N. Basu, Combustion synthesis and characterization of LSCF-based materials as cathode of intermediate temperature solid oxide fuel cells, J. Eur. Ceram. Soc. 29 (2009) 2003–2011. doi:10.1016/j.jeurceramsoc.2008.11.011.

[26] K.C. Patil, Chemistry of Nanocrystalline Oxide Materials: Combustion Synthesis, Properties and Applications, World Scientific (2008)

[27] H. Aliasghari, A.M. Arabi, H. Haratizadeh, A novel approach for solution combustion synthesis of tungsten oxide nanoparticles for photocatalytic and electrochromic applications, Ceram. Int. 46 (2020) 403–414. doi:10.1016/j.ceramint.2019.08.275.

[28] B. Guan, H. Lin, L. Zhu, B. Tian, Z. Huang, Effect of ignition temperature for combustion synthesis on the selective catalytic reduction of NO_x with NH_3 over $Ti_{0.9}Ce_{0.05}V_{0.05}O_2$-$\delta$ nanocomposites catalysts prepared by solution combustion route, Chem. Eng. J. 181–182 (2012) 307–322. doi:10.1016/j.cej.2011.11.083.

[29] J. Zhang, Q. Guo, Y. Liu, Y. Cheng, Preparation and characterization of Fe_2O_3/Al_2O_3 using the solution combustion approach for chemical looping combustion, Ind. Eng. Chem. Res. 51 (2012) 12773–12781. doi:10.1021/ie301804c.

[30] P. Erri, P. Pranda, A. Varma, Oxidizer-fuel interactions in aqueous combustion synthesis. 1. Iron(III) nitrate-model fuels, Ind. Eng. Chem. Res. 43 (2004) 3092–3096. doi:10.1021/ie030822f.

[31] M. Zawadzki, H. Grabowska, J. Trawczyński, Effect of synthesis method of LSCF perovskite on its catalytic properties for phenol methylation, Solid State Ion. 181 (2010) 1131–1139. doi:10.1016/j.ssi.2010.06.009.

[32] R. Mani, R.K. Gautam, S. Banerjee, A.K. Srivastava, A. Jaiswal, M.C. Chattopadhyaya, A study on $La_{0.6}Sr_{0.4}Co_{0.3}Fe_{0.8}O_3$ (LSCF) cathode material prepared by gel combustion method for IT-SOFCs: Spectroscopic, electrochemical and microstructural analysis, Asian J. Res. Chem. 8 (2015) 389. doi:10.5958/0974-4150.2015.00062.0.

[33] D. Huang, Q. Xu, F. Zhang, W. Chen, H. Liu, J. Zhou, Structure and mixed electronic-ionic conducting properties of $La_{0.6}Sr_{0.4}Co_{1-y}Fe_yO_3$(y=0-1.0) ceramics made by a citrate method, J. Wuhan Univ. Technol. Mater. Sci. Ed. 23 (2008) 80–84. doi:10.1007/s11595-006-1080-3.

[34] Robert A. Meyers, Encylopedia of physical science and technology, 3rd Ed. vol. 1 (2001)

[35] A.B. Benipayo, R.B.M. Cervera, Influence of carbon black pore former on the synthesis of lsm-ysz composite electrode material via solid-state reaction and glycine-nitrate process, Mater. Sci. Forum. 950 MSF (2019) 154–159. doi:10.4028/www.scientific.net/MSF.950.154.

[36] L. Zhou, M.R. Zachariah, Size resolved particle work function measurement of free

nanoparticles: aggregates vs. spheres, Chem. Phys. Lett. 525–526 (2012) 77–81. doi:10.1016/j.cplett.2011.11.045.

[37] A. Mezzi, P. Soltani, S. Kaciulis, A. Bellucci, M. Girolami, M. Mastellone, D.M. Trucchi, Investigation of work function and chemical composition of thin films of borides and nitrides, Surf. Interface Anal. 50 (2018) 1138–1144. doi:10.1002/sia.6442.

[38] A. Varma, A.S. Mukasyan, A.S. Rogachev, K. V. Manukyan, Solution combustion synthesis of nanoscale materials, Chem. Rev. 116 (2016) 14493–14586. doi:10.1021/acs.chemrev.6b00279.

[39] S. Chatterjee, S.K. Bhattacharya, Size-dependent catalytic activity and fate of palladium nanoparticles in Suzuki-Miyaura coupling reactions, ACS Omega. 3 (2018) 12905–12913. doi:10.1021/acsomega.8b01598.

[40] A. Staykov, H. Tellez, J. Druce, J. Wu, T. Ishihara, J. Kilner, Electronic properties and surface reactivity of SrO-terminated $SrTiO_3$ and SrO-terminated iron-doped $SrTiO_3$, Sci. Technol. Adv. Mater. 19 (2018) 221–230. doi:10.1080/14686996.2018.1440136.

[41] A.P. Jamale, C.H. Bhosale, L.D. Jadhav, Effect of screen-printing mesh opening diameter on microstructural and electrical properties of $La_{0.6}Sr_{0.4}Co_{0.2}Fe_{0.8}O_3$-$\delta$ thick films, J. Electron. Mater. 45 (2015) 509–514. doi:10.1007/s11664-015-4139-0.

[42] R.M. Navarro, M.C. Alvarez-Galvan, J.A. Villoria, I.D. González-Jiménez, F. Rosa, J.L.G. Fierro, Effect of Ru on $LaCoO_3$ perovskite-derived catalyst properties tested in oxidative reforming of diesel, Appl. Catal. B Environ. 73 (2007) 247–258. doi:10.1016/j.apcatb.2006.12.013.

[43] A.P. Jamale, S.T. Jadhav, S.U. Dubal, C.H. Bhosale, L.D. Jadhav, Studies on the percolation limit of $Ce_{0.9}Gd_{0.1}O_{1.95}$ in $La_{0.6}Sr_{0.4}Co_{0.2}Fe_{0.8}O_3$-$\delta$-$Ce_{0.9}Gd_{0.1}O_{1.95}$ nanocomposites for solid oxide fuel cells application, J. Phys. Chem. Solids. 85 (2015) 96–101. doi:10.1016/j.jpcs.2015.05.012.

[44] V. Esposito, C. Gadea, J. Hjelm, D. Marani, Q. Hu, K. Agersted, S. Ramousse, S.H. Jensen, Fabrication of thin yttria-stabilized-zirconia dense electrolyte layers by inkjet printing for high performing solid oxide fuel cells, J. Power Sources. 273 (2015) 89–95. doi:10.1016/j.jpowsour.2014.09.085.

[45] Q. Meng, W. Wang, X. Weng, Y. Liu, H. Wang, Z. Wu, Active oxygen species in $La_{n+1}Ni_nO_{3n+1}$ layered perovskites for catalytic oxidation of toluene and methane, J. Phys. Chem. C. 120 (2016) 3259–3266. doi:10.1021/acs.jpcc.5b08703.

[46] Y. Yu, H. Luo, D. Cetin, X. Lin, K. Ludwig, U. Pal, S. Gopalan, S. Basu, Effect of atmospheric CO_2 on surface segregation and phase formation in $La_{0.6}Sr_{0.4}Co_{0.2}Fe_{0.8}O_{3-\delta}$ thin films, Appl. Surf. Sci. 323 (2014) 71–77. doi:10.1016/j.apsusc.2014.09.019.

[47] J. Hong, S.J. Heo, A.N. Aphale, B. Hu, P. Singh, H_2O absorption assisted Sr-segregation in strontium nickel oxide based chromium getter and encapsulation with $SrCO_3$, J. Electrochem. Soc. 166 (2019) F59–F65. doi:10.1149/2.0351902jes.

[48] M.R. Ardigò, A. Perron, L. Combemale, O. Heintz, G. Caboche, S. Chevalier, Interface reactivity study between $La_{0.6}Sr_{0.4}Co_{0.2}Fe_{0.8}O_3-\delta$ (LSCF) cathode material and metallic interconnect for fuel cell, J. Power Sources. 196 (2011) 2037–2045. doi:10.1016/j.jpowsour.2010.09.063.

[49] M. Albino, P. Veber, S. Pechev, M. Maglione, Growth and characterization of $Ba_2LnFeNb_4O_{15}$ (Ln = Pr, Nd, Sm, Eu) relaxor single crystals, Cryst. Growth Des. 14 (2014) 500. doi:10.1021/cg401181j.

[50] A.P. Jamale, S.U. Dubal, S.P. Patil, C.H. Bhosale, L.D. Jadhav, Influence of substrate temperature on structural, morphological and electrical properties of $La_{0.6}Sr_{0.4}Co_{0.2}Fe_{0.8}O_3$ thin films for IT-SOFCs, Appl. Surf. Sci. 286 (2013) 78–82. doi:10.1016/j.apsusc.2013.09.020.

[51] R.I. Tomov, T. Mitchell-Williams, C. Gao, R.V. Kumar, B.A. Glowacki, Performance optimization of LSCF/Gd:CeO_2 composite cathodes via single-step inkjet printing infiltration, J. Appl. Electrochem. 47 (2017) 641–651. doi:10.1007/s10800-017-1066-1.

[52] A.P. Jamale, C.H. Bhosale, L.D. Jadhav, Electrochemical behavior of LSCF/GDC interface in symmetric cell: an application in solid oxide fuel cells, J. Alloys Compd. 623 (2015) 136–139. doi:10.1016/j.jallcom.2014.10.122.

[53] S.P. Simner, J.F. Bonnett, N.L. Canfield, K.D. Meinhardt, V.L. Sprenkle, J.W. Stevenson, Optimized lanthanum ferrite-based cathodes for anode-supported SOFCs,

Electrochem. Solid-State Lett. 5 (2002) 173–175. doi:10.1149/1.1483156.

[54] Y. Xu, S. Wang, L. Shao, T. Wen, Z. Wen, Performance of an anode-supported tubular solid oxide fuel cells stack with two single cells connected by a co-sintered ceramic interconnector, Int. J. Hydrogen Energy. 36 (2011) 6194–6198. doi:10.1016/j.ijhydene.2011.01.084.

[55] M. Canavar, Y. Kaplan, Effects of mesh and interconnector design on solid oxide fuel cell performance, Int. J. Hydrogen Energy. 40 (2015) 7829–7834. doi:10.1016/j.ijhydene.2014.11.101.

[56] G.F. Alvarez, M. Mamlouk, S.M. Senthil Kumar, K. Scott, Preparation and characterisation of carbon-supported palladium nanoparticles for oxygen reduction in low temperature PEM fuel cells, J. Appl. Electrochem. 41 (2011) 925–937. doi:10.1007/s10800-011-0318-8.

[57] A.A. Fedotov, S.A. Grigoriev, P. Millet, V.N. Fateev, Plasma-assisted Pt and Pt-Pd nano-particles deposition on carbon carriers for application in PEM electrochemical cells, Int. J. Hydrogen Energy. 38 (2013) 8568–8574. doi:10.1016/j.ijhydene.2012.10.042.

[58] A. Kucernak, F. Bidault, G. Smith, Membrane electrode assemblies based on porous silver electrodes for alkaline anion exchange membrane fuel cells, Electrochim. Acta. 82 (2012) 284–290. doi:10.1016/j.electacta.2012.03.027.

[59] H. Hu, M. Liu, Interfacial studies of solid-state cells based on electrolytes of mixed ionic-electronic conductors, Solid State Ion. 109 (1998) 259–272. doi:10.1016/s0167-2738(98)00095-2.

[60] M. Liu, Z. Wu, Significance of interfaces in solid-state cells with porous electrodes of mixed ionic-electronic conductors, Solid State Ion. 107 (1998) 105–110. doi:10.1016/s0167-2738(97)00528-6.

[61] S.P. Jiang, A comparison of O2 reduction reactions on porous (La,Sr)MnO$_3$ and (La,Sr)(Co,Fe)O$_3$ electrodes, Solid State Ion. 146 (2002) 1–22. doi:10.1016/S0167-2738(01)00997-3.

[62] D.S. Mebane, Y. Liu, M. Liu, A two-dimensional model and numerical treatment for mixed conducting thin films, J. Electrochem. Soc. 154 (2007) A421. doi:10.1149/1.2710204.

[63] R. Das, D. Mebane, E. Koep, M. Liu, Modeling of patterned mixed-conducting electrodes and the importance of sheet resistance at small feature sizes, Solid State Ion. 178 (2007) 249–252. doi:10.1016/j.ssi.2006.12.021.

[64] D.N. Mueller, M.L. MacHala, H. Bluhm, W.C. Chueh, Redox activity of surface oxygen anions in oxygen-deficient perovskite oxides during electrochemical reactions, Nat. Commun. 6 (2015). doi:10.1038/ncomms7097.

[65] J. Janek, M. Martin, K.D. Becker, Physical chemistry of solids - the science behind materials engineering, Phys. Chem. Chem. Phys. 11 (2009) 3010. doi:10.1039/b905911n.

[66] A.J. Gatesman, R.H. Giles, J. Waldman, High-precision reflectometer for submillimeter wavelengths, J. Opt. Soc. Am. B. 12 (1995) 212. doi:10.1364/josab.12.000212.

[67] S.P. Jiang, J.G. Love, L. Apateanu, Effect of contact between electrode and current collector on the performance of solid oxide fuel cells, Solid State Ion. 160 (2003) 15–26. doi:10.1016/S0167-2738(03)00127-9.

[68] J. Chen, F. Liang, B. Chi, J. Pu, S.P. Jiang, L. Jian, Palladium and ceria infiltrated $La_{0.8}Sr_{0.2}Co_{0.5}Fe_{0.5}O_3$-δ cathodes of solid oxide fuel cells, J. Power Sources. 194 (2009) 275–280. doi:10.1016/j.jpowsour.2009.04.041.

[69] V.C. Kournoutis, F. Tietz, S. Bebelis, AC impedance characterisation of a $La_{0.8}Sr_{0.2}Co_{0.2}Fe_{0.8}O_3$-δ electrode, Fuel Cells. 9 (2009) 852–860. doi:10.1002/fuce.200800120.

[70] Özden Çelikbilek, E. Siebert, D. Jauffrès, C.L. Martin, E. Djurado, Influence of sintering temperature on morphology and electrochemical performance of LSCF/GDC composite films as efficient cathode for SOFC, Electrochim. Acta. 246 (2017) 1248–1258. doi:10.1016/j.electacta.2017.06.070.

Figures

Fig. 1. Photograph of combustion reaction taking place at fuel to oxidant ratio (ψ) of 2.0.
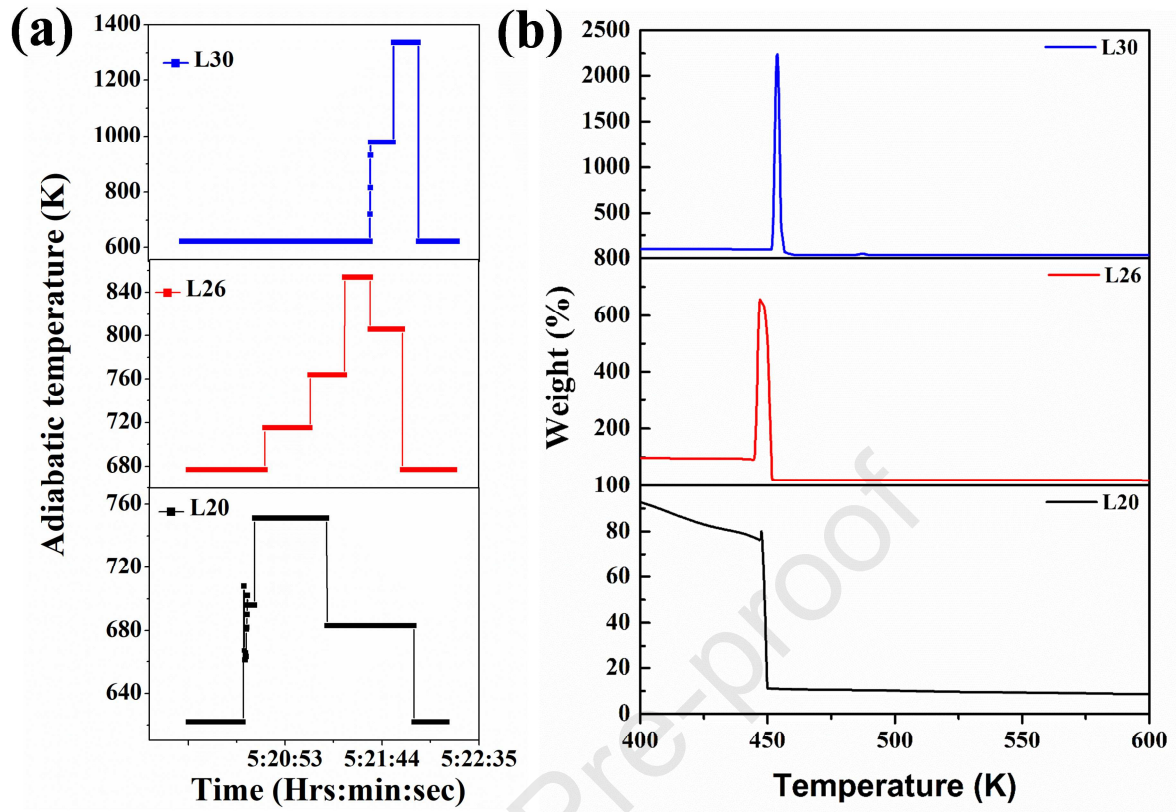
Fig. 2. (a) Temperature vs time profiles of combustion reaction determined from IR-pyrometer instrument, and (b) the thrust detected in TGA of gel at different fuel to oxidant ratios (ψ) of 2.0, 2.6, and 3.0.
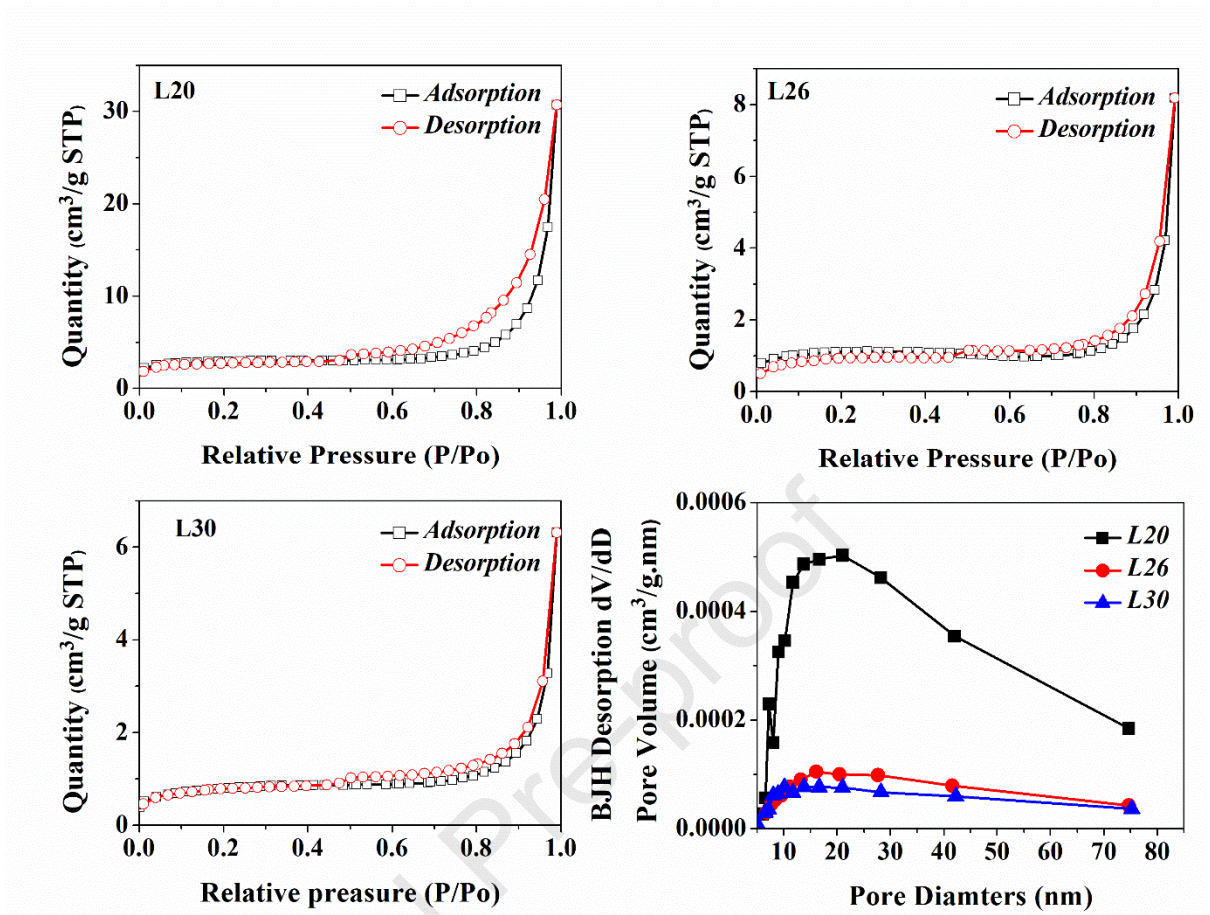
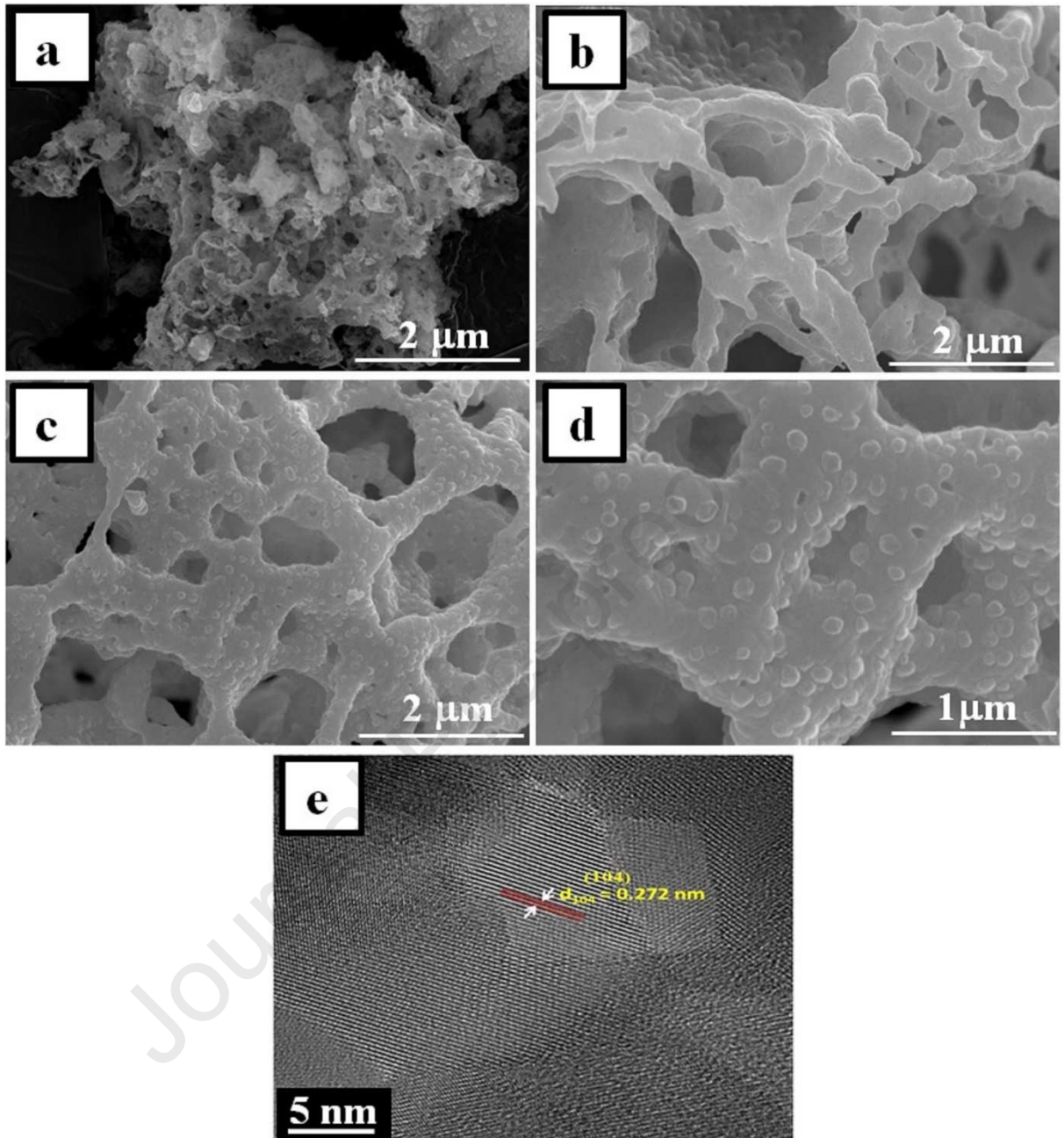**Fig. 3.** N_2-adsorption–desorption isotherms and pore size distributions of L20 [19], L26, and L30 powders.

Fig. 4. FE-SEM images of (a) L20, (b) L26, and (c) L30 powders; (d) higher magnified FE-SEM image of L30; and (e) TEM image of L20 powder.
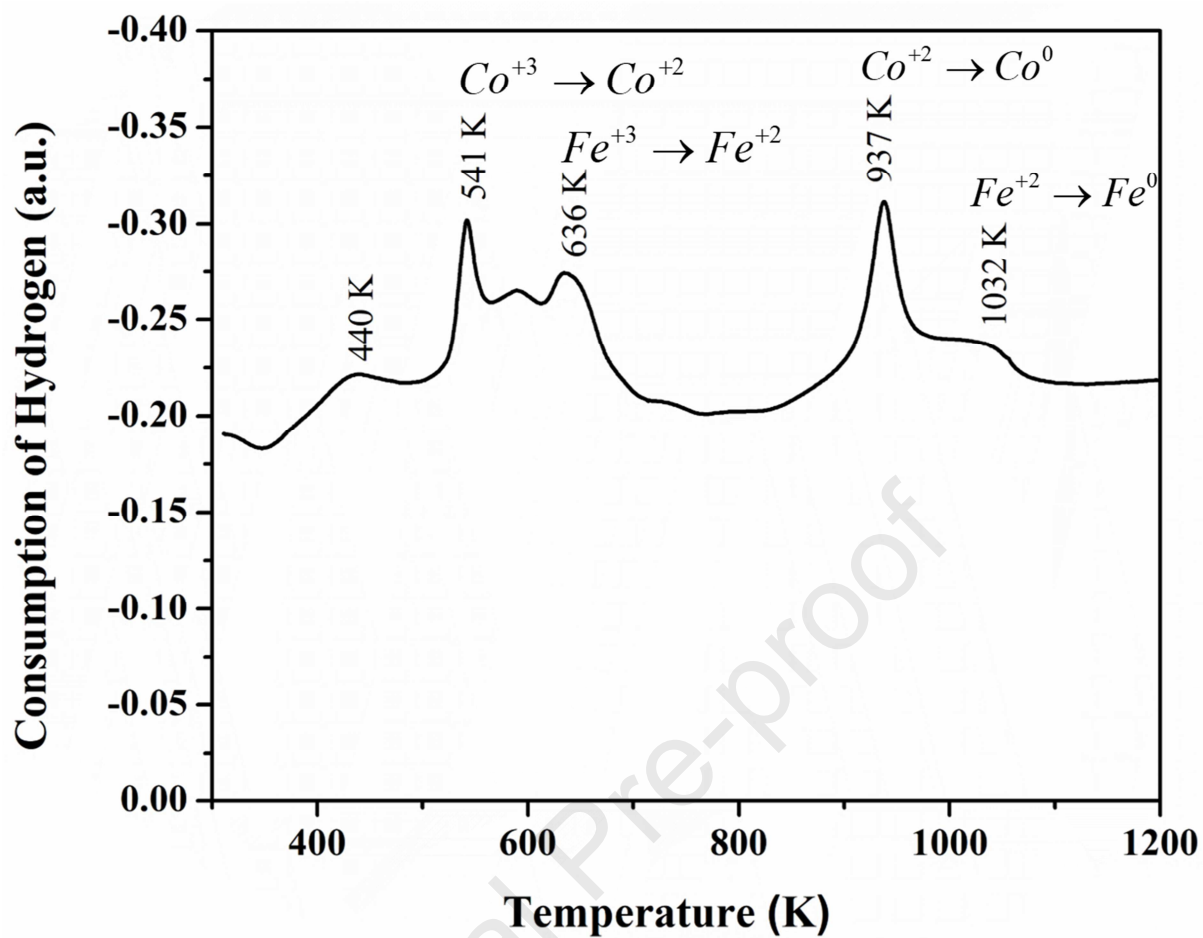
Fig. 5. H$_2$-TPR spectrum of L20 sample.
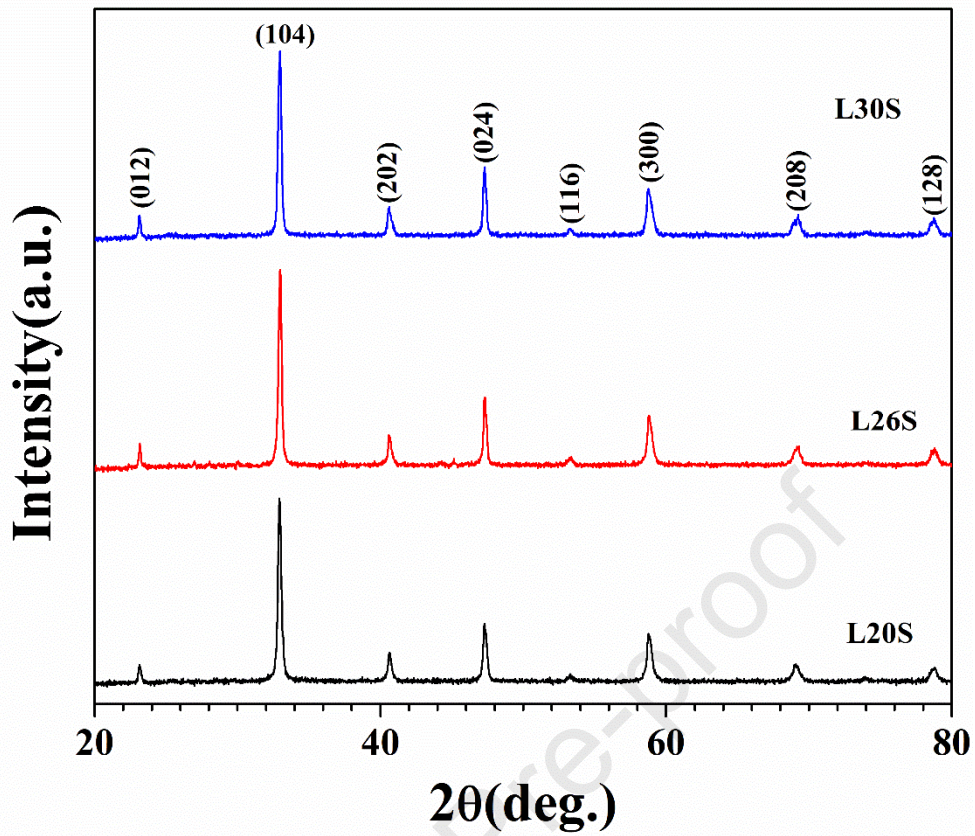
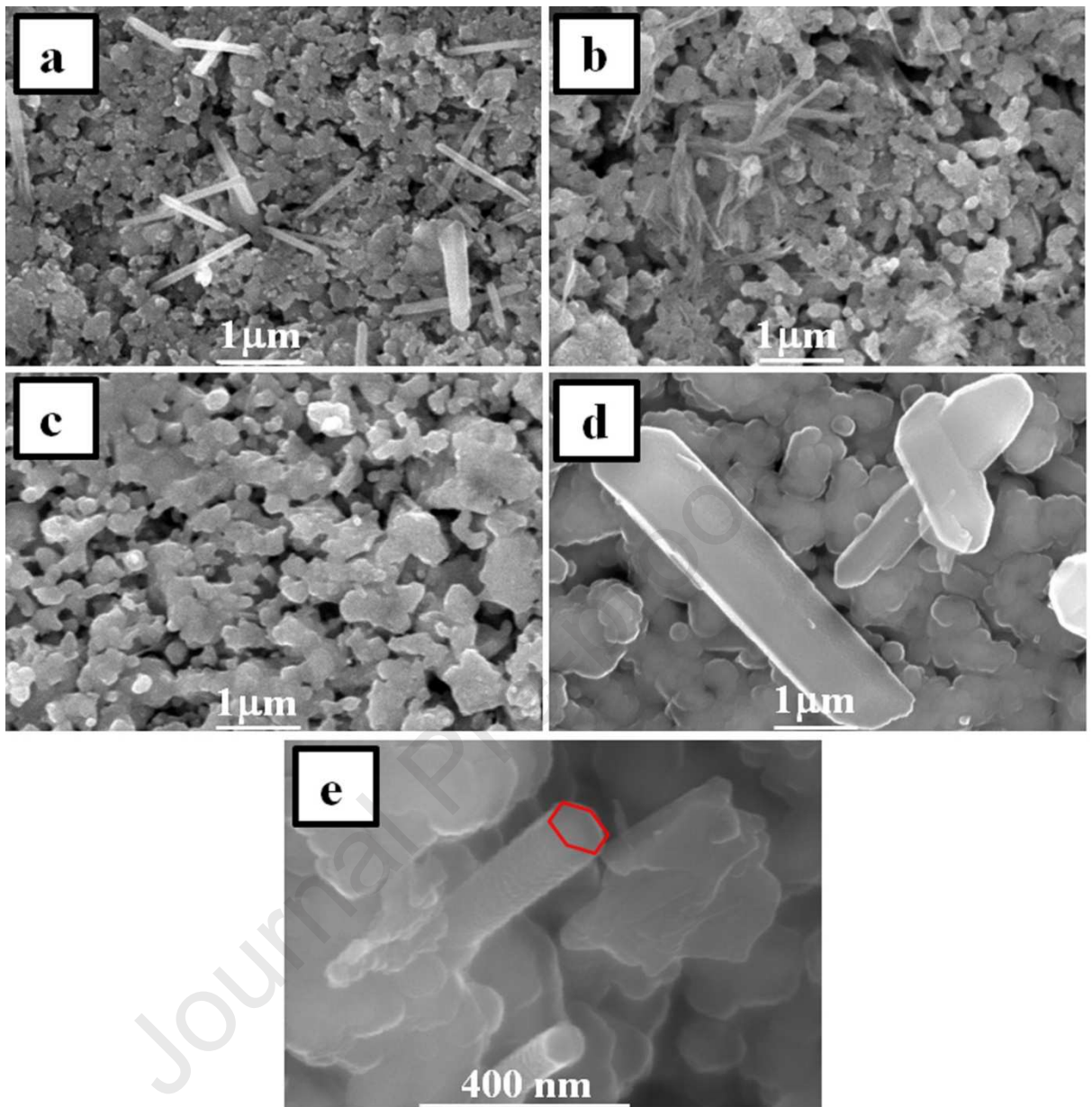**Fig. 6.** XRD patterns of L20S, L26S, and L30S pellets.

Fig. 7. Surface SEM micrographs of (a) L20S, (b) L26S, and (c) L30S pellets; and magnified
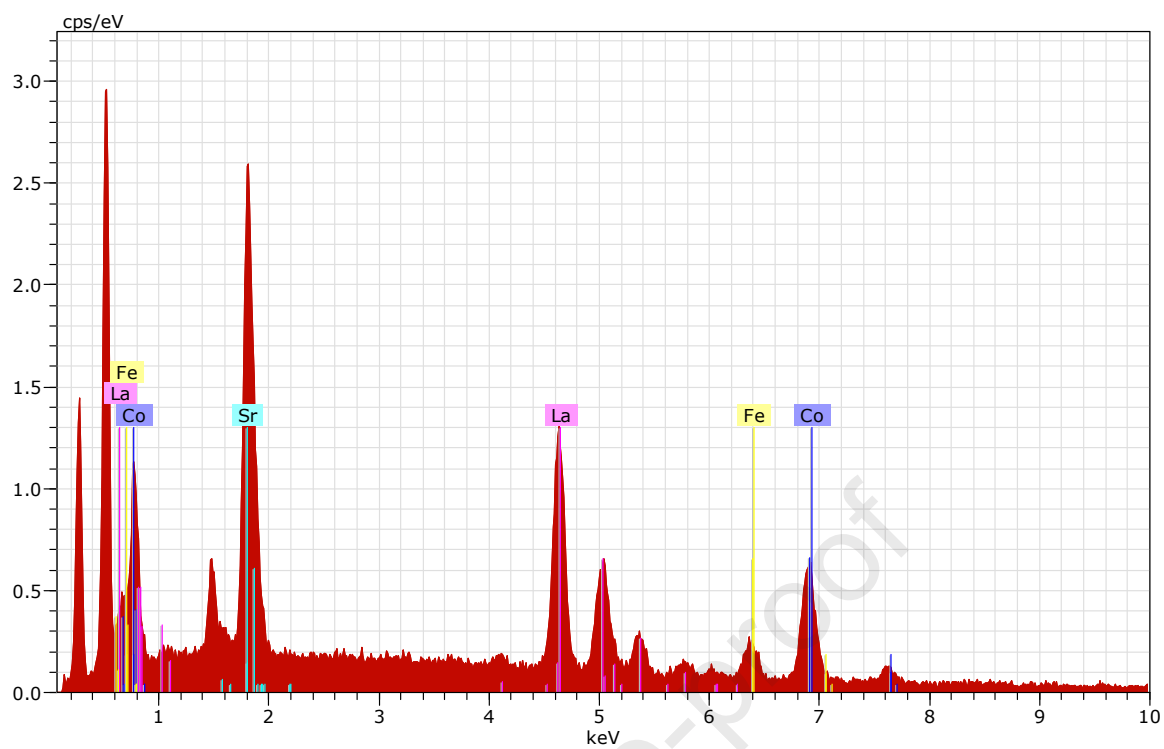SEM micrographs of surface (d) and cross-section (e) of the L20S sample.

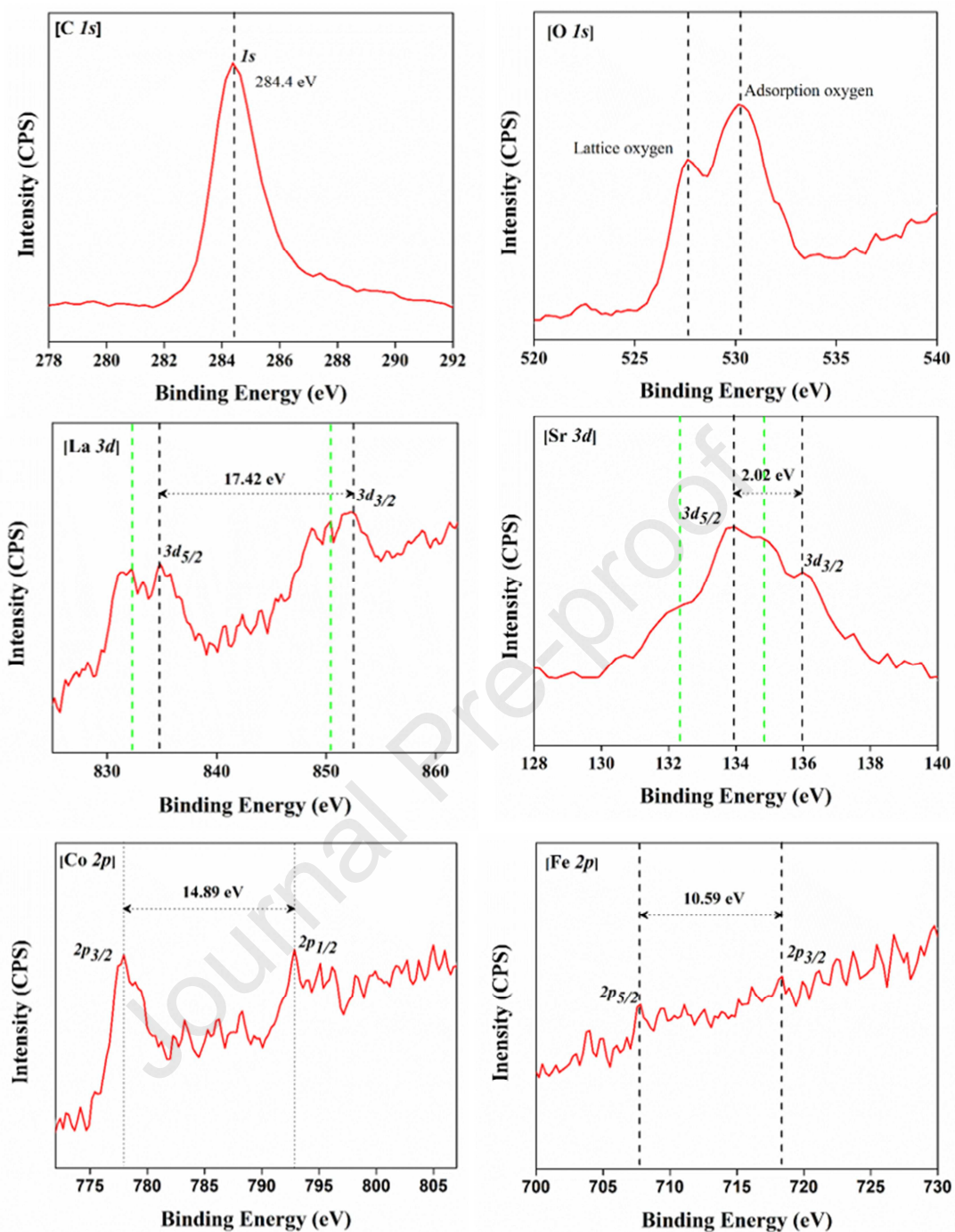**Fig. 8.** EDS spectra captured on the nanorod of L20S sample.

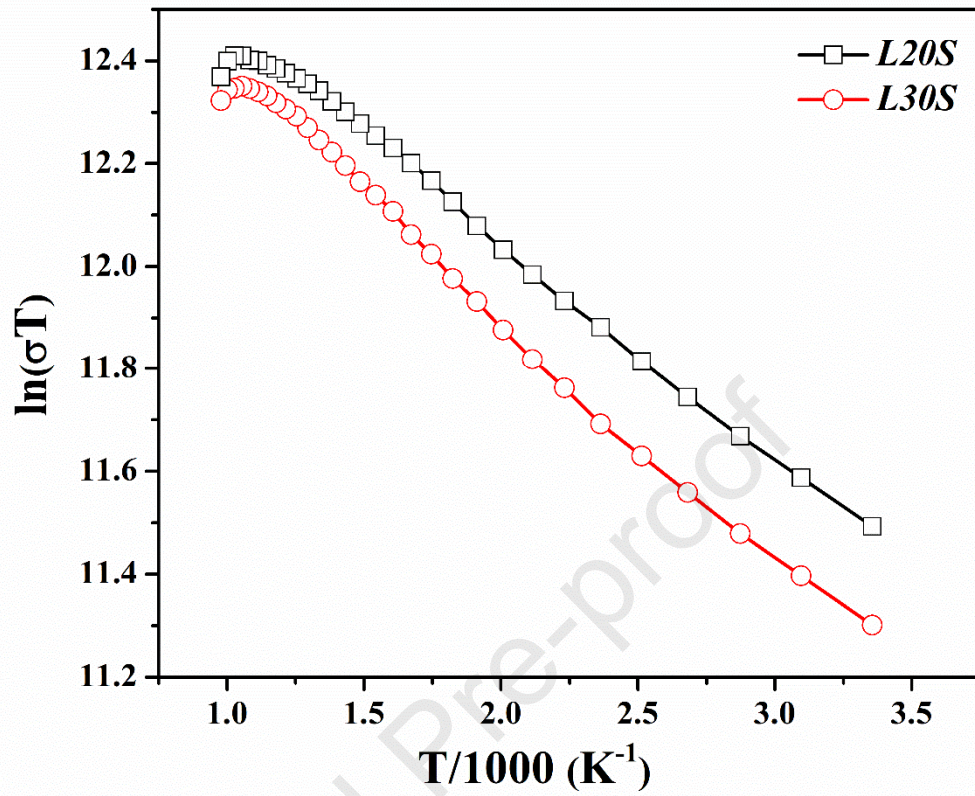**Fig. 9.** X-ray photoelectron spectra of L20S sample.

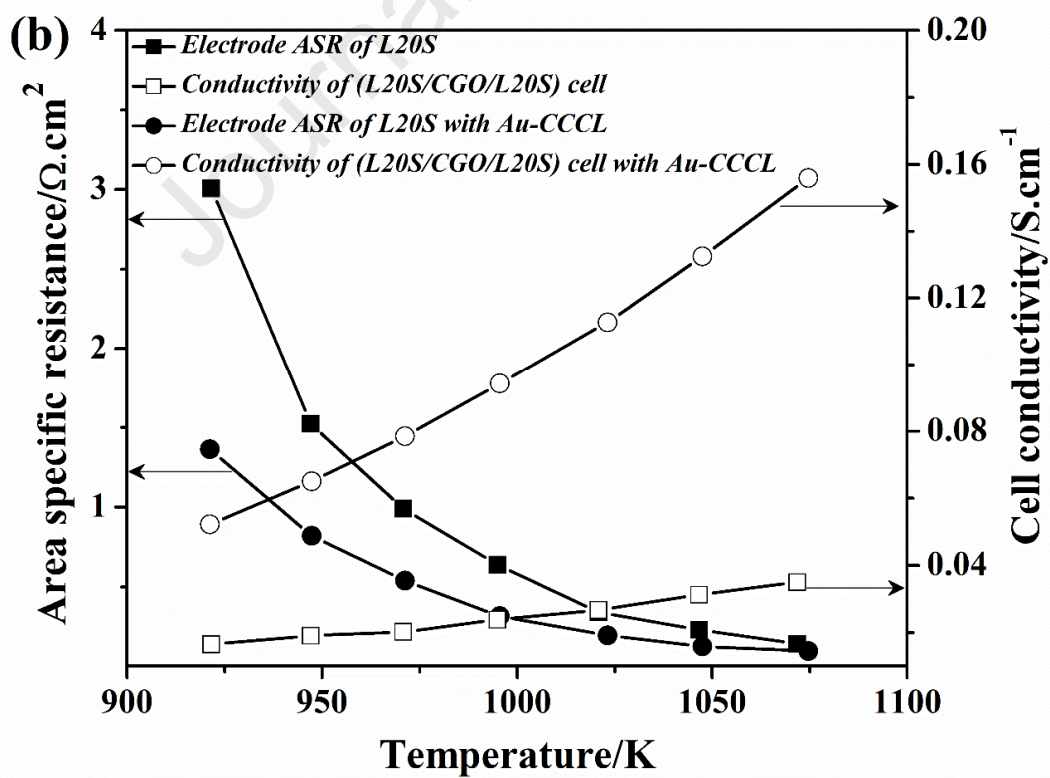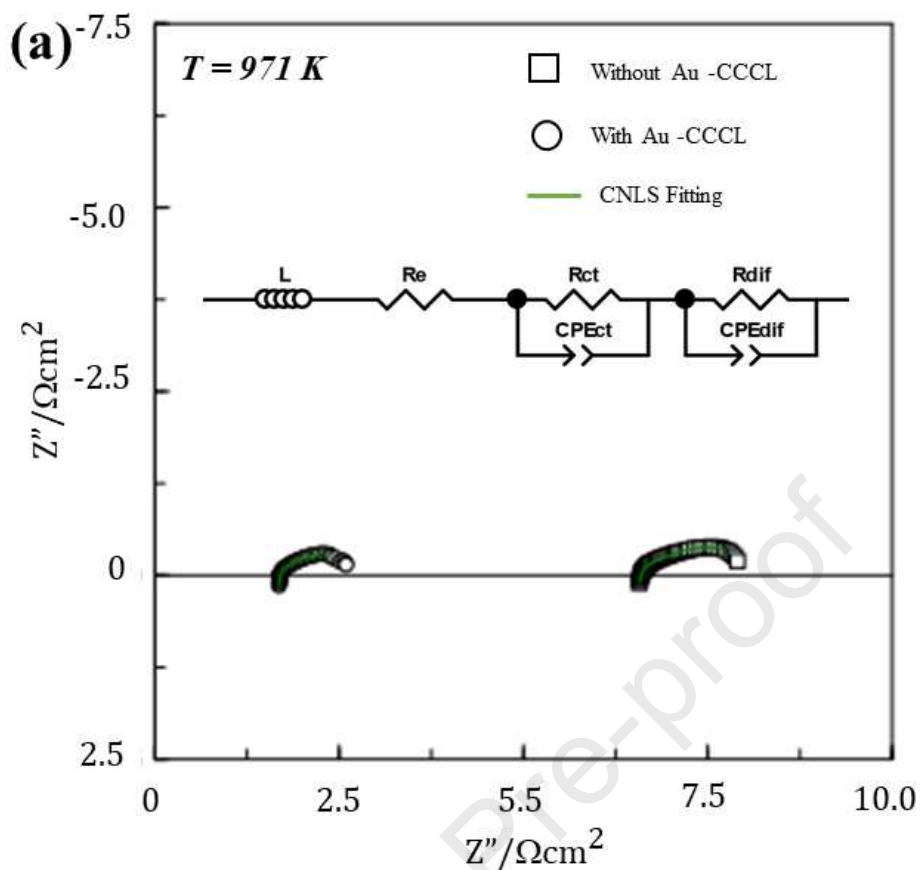**Fig. 10.** DC electrical conductivity of L20S and L30S samples.

Fig. 11. (a) EIS spectra of L20S electrodes without and with the use of Au–CCCL at 971 K, in air, with an equivalent circuit used in fitting the data shown in inset; (b) plots of the electrode area specific resistance and the cell conductivity results obtained in symmetrical cells.

Tables

Table 1 Sample acronyms, fuel to oxidant ratio, adiabatic temperature, hydrodynamic radius, and BET surface area of samples synthesized at various fuel conditions.

Sample acronym	Fuel to oxidant ratio (ψ)	Adiabatic temp. (K)	Hydrodynamic radius (nm)	BET surface area ($m^2 g^{-1}$)
L20	Deficient	751	598	10.97
L26	Stoichiometric	854	825	4.12
L30	Rich	1337	1111	2.84

Table 2 Sample acronyms, crystallite size, d_{100} interplanar spacing, and Archimedes, X-ray, and relative densities of samples sintered at 1000 °C for 2 h.

Sample	Crystallite size (nm)	d_{100} (Å)	Density		
			Archimedes (g cm^{-1})	X-ray (g cm^{-1})	Relative (%)
L20S	27.65	2.7185	6.20	6.64	93.37
L26S	27.60	2.7135	5.98	6.62	90.33
L30S	27.60	2.7145	5.73	6.54	87.61

Table 3 Elemental analysis estimated from XPS and EDS spectra of the surface and nanorods of L20S sample, respectively.

Elemental composition (%)					La:Sr	Co:Fe
Elements	La	Sr	Co	Fe		
XPS surface	23.59	26.20	40.31	9.88	0.90	4.07
EDS rod	19.93	45.00	27.25	7.34	0.44	3.71
Precursor	30	20	40	10	1.5	4

35

Highlights:

- Propellant chemistry detailed for active electrode synthesis

- Glycine–nitrate process retained a maximum reaction temperature of 1337 K

- Nanocrystalline $La_{0.6}Sr_{0.4}Co_{0.8}Fe_{0.2}O_{3-\delta}$ ensured in as-synthesized powder by HR-TEM

- Large electrode surface area, 10.97 $m^2\,g^{-1}$, resulted in excellent H_2-TPR activity

- EIS showed the catalytic current collector requirement for SOFC electrode

Declaration of interests

The authors declared that they have no conflicts of interest to this work. We further declare that we do not have any commercial or associative interest that represents a conflict of interest in connection with the submitted work.

<div align="right">

Dr. Atul Jamale
2020-03-28

</div>